Electronic Supplementary Material (ESI) for ChemComm.

Supplementary Information

Mixed-Oxide-Containing Composite-Supported MoPt with Ultralow Pt Content for Accelerating Hydrogen Evolution Performance

EXPERIMENTAL DETAILS

Chemical reagents

All reagents were commercially purchased and used without further purification. Titanium tetrachloride ($TiCl_4$, 99.9%) and iridium trichloride hydrate ($IrCl_3.xH_2O$, 99.9%) were obtained from Aladdin (China) and Sigma-Aldrich (USA), respectively. Hydrochloric acid (HCl, 37%), ethylene glycol ($(CH_2OH)_2$, 99.0%), sodium hydroxide (NaOH, ≥ 99.0%), and sodium borohydride ($NaBH_4$, 98.0%) were purchased by Merck, Germany. Chloroplatinic acid hexahydrate ($H_2PtCl_6.6H_2O$, ≥37.50% Pt basis) and molybdenum(V) chloride ($MoCl_5$, 95.0%) were bought from Sigma-Aldrich, USA. Vulcan carbon black (XC-72) was achieved from Fuel Cell Store, USA.

Synthesis of activated Vulcan XC-72

The Vulcan carbon black (XC-72) was pre-treated in HNO_3 solution at room temperature for 12 hours to remove other impurities and introduce functional groups on the carbon surface. After the acidization, the resultant precipitation was collected by centrifugation and washing at least repeated 10 times until the solution became neutral, followed by drying at 80 ^oC in air.

Synthesis of rutile $Ti_{0.9}Ir_{0.1}O_2$ nanoparticle

The rutile $Ti_{0.9}Ir_{0.1}O_2$ nanoparticle was prepared by a hydrothermal process, which is firstly reported by our groups.[1] Briefly, 0.07 g of $IrCl_3.xH_2O$ was dissolved completely into 50 mL of purged H_2O, followed by adjusting the pH value to 0 using HCl solution. Afterward, 0.2 mL of $TiCl_4$ was dropped into the above solution and then put into a Teflon-lined autoclave, being heated to 210 ^oC for 12 hours. The resulting product was collected by centrifugation, washing, and drying at 80 ^oC overnight.

Synthesis of rutile $Ti_{0.9}Ir_{0.1}O_2$-C nanocomposite

The rutile $Ti_{0.9}Ir_{0.1}O_2$-C (50: 50 wt%) nanocomposite was fabricated by a simple and facile chemical method. Firstly, 0.025 g of activated Vulcan XC-72 carbon and 0.025 g of rutile

$Ti_{0.9}Ir_{0.1}O_2$ nanoparticle were dropped into 50 mL of a solution containing ethylene glycol and isopropyl alcohol (4: 1 volume ratio), followed by ultrasonication for 15 min to form a homogenous suspension. Afterward, the obtained suspension was put on a Teflon-lined autoclave and was heated at 120 ^oC for 8 hours. Next, the precipitation was washed and centrifuged with acetone and water to remove completely organic solvents at least repeated 10 times and was dried at 80 ^oC overnight.

Synthesis of the MoPt/$Ti_{0.9}Ir_{0.1}O_2$-C catalyst

The MoPt/$Ti_{0.9}Ir_{0.1}O_2$-C electrocatalyst was prepared by a facile chemical reduction process. In a typical experiment, 23.4 mg of $Ti_{0.9}Ir_{0.1}O_2$-C nanocomposite was distributed into a solution containing 25 mL of H_2O and 5 mL of ethylene glycol and was ultrasonicated for 30 min. Afterward, 0.21 mL of H_2PtCl_6 (0.02 M) and 0.07 mL of $MoCl_5$ (0.02 M) were quickly dropped into the above suspension under vigorous stirring for 5 min, followed by modulating the pH value to 11 by NaOH (1 M). After stirring the suspension for 15 min, 5 mL of $NaBH_4$ reductant was injected slowly into and stirred continuously for 2 hours at room temperature for the complete reduction reaction. The product was collected by centrifugation, washing, and drying in air at 80 ^oC for further use.

Material Characterizations

X-ray diffraction (XRD) pattern of all studied nanomaterials was collected on D2 PHASER (Bruker, Germany) with Cu K_α radiation source (λ = 1.5418 Å) in 2θ range from 20^o – 80^o at a step size of 0.02^o. Fourier-transform infrared (FT-IR) spectra were acquired on Nicolet iS5 FT-IR Spectrometer devices (Thermo Scientific, USA) with scanning from 4000 to 400 cm^{-1} at room temperature Field emission scanning electron microscopes (FE-SEM) coupled with energy dispersive X-ray analysis (EDX) mapping was conducted on JOEL-JSM 6500F device at 15 kV to record the composition and distribution of elements in the as-obtained samples. High-resolution transmission electron microscopy (HR-TEM) images of as-prepared

nanomaterials were collected on a JOEL-JEM 2100F device at 200 kV. Scanning transmission electron microscopy (STEM) and elemental mapping were carried out on a JOEL-JED 2300T device. X-ray photoelectron spectroscopy (XPS) was performed on PHI 5000 VersaProbe (Ulvac-PHI) equipped with a monochromator Al K_α (h^υ = 1486.6 eV) X-ray source.

Electrochemical Investigations

Electrochemical measurements were conducted on an Autolab potentiostat/galvanostat (PGSTAT302N) workstation (Metrohm Co., Ltd. Switzerland) coupled with a three-electrode cell, including a working electrode (glassy carbon (GCE), 3 mm), a counter electrode (platinum wire), and reference electrode (Ag/AgCl/(sat.KCl). Before electrochemical tests, the catalyst ink was prepared by dispersion of 1.7 mg of as-made catalyst in a mixture of 20 µL of Nafion and 80 µL of isopropyl alcohol, and then 30 min ultrasonication to generate a homogeneous ink. Before coasting the as-prepared catalyst ink, the GCE surface was polished with 0.5 µm Al_2O_3 and washed with absolute ethanol and purged water, followed by dropping 2.5 µL of catalyst ink onto the GCE surface and drying naturally. To start with, a cyclic voltammetry test was performed in an N_2-saturated 0.5 M H_2SO_4 electrolyte solution with 100 cycles at 50 mV s^{-1} to get an active working electrode. Linear sweep voltammetry (LSV) was conducted to record polarization curves toward hydrogen evolution reaction (HER) in 0.5 M H_2SO_4 electrolyte at a scan rate of 5 mV s^{-1}. Electrochemical impedance spectroscopy (EIS) was recorded in a frequency range of 0.1 - 10^5 Hz at HER potential in 0.5 M H_2SO_4 electrolyte. To evaluate the electrocatalytic stability, an accelerated durability test (ADT) with 5000-cycling was conducted in 0.5 M H_2SO_4 solution. In addition, the chronopotentiometry (CP) test also was conducted in 0.5 M H_2SO_4 electrolyte at a constant current density of -10 mA cm^{-2} and 10 mA cm^{-2} to further durability of all investigated electrocatalysts for the HER process at 10 hours. For comparison, Pt/C (E-TEK) was used as benchmark catalysts for HER. All reported potentials were converted from Ag/AgCl to reversible hydrogen electrode (RHE) scale by Eqs.

(1)-(3):[2]

$$E_{RHE} = E_{Mea} + 0.059*pH + E^{0}_{Ag/AgCl} \quad (1)$$

$$E_{RHE} = E_{Mea} + 0.059*0 + 0.197 \quad (2)$$

$$E_{RHE} = E_{Mea} + 0.197 \quad (3)$$

where E_{RHE} is a potential versus RHE, E_{Mea} is a measured potential, $E^{0}_{Ag/AgCl}$ is a standard electrode potential of Ag/AgCl/(sat.KCl), and pH of 0.5 M H_2SO_4 is close to 0.

Calculation of electrochemical surface area (ECSA)

The active surface area of investigated electrocatalysts was calculated from their double-layer capacitance (C_{dl}). The electrical capacitance between the double layers was calculated from the cyclic voltammetry curves with a narrow potential window from 0.35 V_{RHE} to 0.45 V_{RHE} at various scan rates (10, 20, 40, 60, 80, and 100 mV s^{-1}) by following Eq. (5):[3, 4]

$$\Delta j / 2 = \left(j_a - j_c\right) / 2 = \nu \times C_{dl} \quad (4)$$

where ν (mV s^{-1}) is a scan rate; j_a (mA cm^{-2}) and j_c (mA cm^{-2}) are current density at anodic and cathodic scans, respectively; C_{dl} (mF cm^{-2}) is a double-layer capacitance. The double-layer capacitance (C_{dl}) can be determined from the plots of half of the capacitive current density ($(\Delta j/2)$ against scan rates. The ECSA value was calculated from the double-layer capacitance according to Eq. (6):[4-6]

$$ECSA = \frac{C_{dl}}{C_S \text{ per } cm^2_{ECSA}} \quad (5)$$

Where C_{dl} (mF cm^{-2}) is the double-layer capacitance; $C_S \text{ per } cm^2_{ECSA}$ is the specific capacitance of a planar surface, assigned to be 0.04 mF cm^{-2} with a standard 1 cm^{-2} real surface area.[6-8]

Calculation of turnover frequency (TOF)

The per-site turnover frequency (TOF) of investigated electrocatalysts was calculated according to the following Eq. (7 - 9) as reported in previous studies:[6, 9-15]

$$TOF\ per\ site = \frac{\#total\ hydrogen\ turnovers\ per\ geometric\ area}{\#active\ sites\ per\ geometric\ area} \quad (6)$$

The number of total hydrogen turnovers is calculated from the current density extracted from the linear sweep voltammetry (LSV) curves by the following Eq. (6):

$$\#H_2 = \left(|j|\frac{mA}{cm^2}\right)\left(\frac{1\ C\ s^{-1}}{1000\ mA}\right)\left(\frac{1\ mol\ e^{-1}}{96485.3\ C}\right)\left(\frac{1\ mol\ H_2}{2\ mol\ e^{-1}}\right)\left(\frac{6.022 \times 10^{23}\ H_2\ molec}{1\ mol\ H_2}\right) \quad (7)$$

$$= 3.12 \times 10^{15}\frac{H_2/s}{cm^2}\ per\ \frac{mA}{cm^2}$$

The number of active sites of investigated catalysts was estimated from the mass loading on the working electrode surface, Pt content, and atomic Pt weight with the assumption each Pt center accounts for one active site:

$$\#active\ sites = \left(\frac{catalyst\ loading\ per\ ge}{M}\right) \quad (8)$$

Calculation of Tafel slope

The Tafel slope of all investigated electrocatalysts was calculated in the Tafel plots, which was fitted by the Tafel equation, as shown in Eq. (4):[16, 17]

$$\eta = b \times logj + a = \frac{2.3 \times R \times T}{\alpha \times n \times F} logj - \frac{2.3 \times R \times T}{\alpha \times n \times F} logj_0 \quad (9)$$

where R and T (K) present gas constant and absolute temperature, respectively; α denotes a charge transfer co-efficient, F presents a Faraday constant; and j_0 (mA cm^{-2}) is an exchange current density.

Results and Discussion

Characterization of $Ti_{0.9}Ir_{0.1}O_2$-C composite

X-ray diffraction (XRD) was conducted to investigate the crystalline structure of the as-constructed catalyst supports. As presented in Figure S1, the XRD pattern of activated carbon support showed two diffraction peaks at nearly 25° and 43°, corresponding to the (002) and (100) planes of the carbon structure.[18] The XRD profile of the $Ti_{0.9}Ir_{0.1}O_2$ demonstrated representative reflection peaks at 27.41° (110), 36.07° (101), 41.22° (111), 44.01° (210), 54.33° (211), 56.64° (220), 69.01° (112), and 69.79° (311), being slightly shifted to angle higher than those of standard rutile TiO_2 structure (JCPDS 76-1940), and no peaks analogous to the anatase structure were detected. This suggested the formation of the single rutile Ir-doped TiO_2 nanomaterial. Apart from the diffraction peaks at the same position of the $Ti_{0.9}Ir_{0.1}O_2$ support, the XRD pattern of the $Ti_{0.9}Ir_{0.1}O_2$-C composite support showed the margination between the (002) plane of activated carbon and the (110) plane of the $Ti_{0.9}Ir_{0.1}O_2$, increasing the intensity of the diffraction peak at 27.41° compared to that of the $Ti_{0.9}Ir_{0.1}O_2$ support.

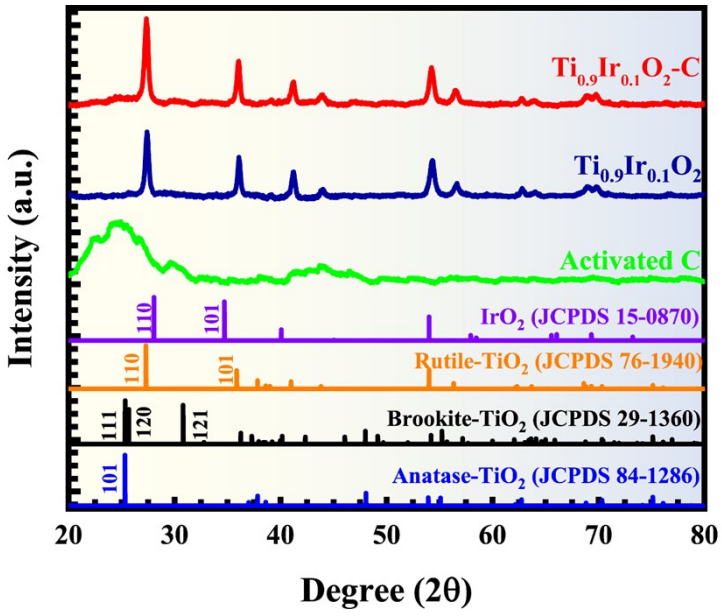

Figure S1. XRD patterns of all investigated supports in the 2θ range from 20° – 80° at a sweep size of 0.02°.

In addition, Fourier transforms infrared (FT-IR) spectra also was conducted to view the formation of functional groups and chemical bonds of the as-obtained $Ti_{0.9}Ir_{0.1}O_2$-C support. Figure 2b depicts that the FT-IR spectra of the $Ti_{0.9}Ir_{0.1}O_2$ support showed absorption peaks at ~3400 cm^{-1} (O-H stretching), ~1700-1320 cm^{-1} (O-H bending) by absorbed water, and ~583 cm^{-1} (Ti-O and/or Ti-O-M stretching vibrations).[19, 20] The position of these vibrational bands were moved slightly to the wavenumber lower than those of pure TiO_2,[19] suggesting the successful doping of Ir atoms into TiO_2 lattices. While the FT-IR spectra of activated carbon support demonstrated various peaks at ~3400 cm^{-1} (O-H stretching), ~1720- 1530 cm^{-1} (O-H bending overlapped with C=C stretching and C=O stretching vibrations), ~1350 cm^{-1} (O-H stretching), and ~1200 cm^{-1} (C-O stretching).[18] The generation of oxygen-containing groups of activated carbon can form intimate contact between activated carbon and $Ti_{0.9}Ir_{0.1}O_2$, resulting in the fine stability of the composites.[19, 20] In addition to the vibrational bands of $Ti_{0.9}Ir_{0.1}O_2$ and activated carbon, the FT-IR spectra of the as-obtained $Ti_{0.9}Ir_{0.1}O_2$-C support showed two new absorption peaks at below 1000 cm^{-1}, corresponding to the of Ti-O-M and Ti-O-C stretching vibrations.[19, 21] These results indicated that the appearance of chemically bound composites of $Ti_{0.9}Ir_{0.1}O_2$ and activated carbon supports was attributable to the interaction between surface oxygen-containing groups of the activated carbon and hydroxyl groups on the surface of the $Ti_{0.9}Ir_{0.1}O_2$ during the formation of composites.[19, 20, 22]

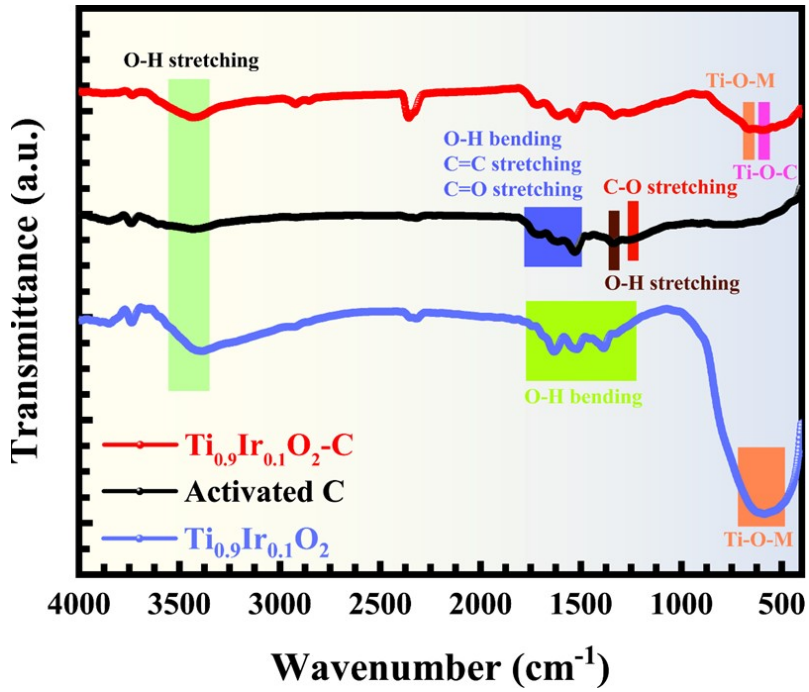

Figure S2. FT-IR spectrums of all supports in the wavenumber of 400 – 4000 cm^{-1}

The FE-SEM/EDX mapping was carried out to verify the morphology, elemental composition, and distribution in the as-made composite. As can be seen in Figure S3 and S4, the FE-SEM image demonstrated the uniformity surface of the as-obtained $Ti_{0.9}Ir_{0.1}O_2$-C support. The EDX mapping showed the well-fine distribution of Ti, O, Ir, and C elements, and the weight ratio of $Ti_{0.9}Ir_{0.1}O_2$: C was 51.24: 48.76 wt.%, which was in agreement with the theoretical ratio (50: 50 wt%), as illustrated in Figure S5. These outcomes demonstrated the formation of the $Ti_{0.9}Ir_{0.1}O_2$-C composite.

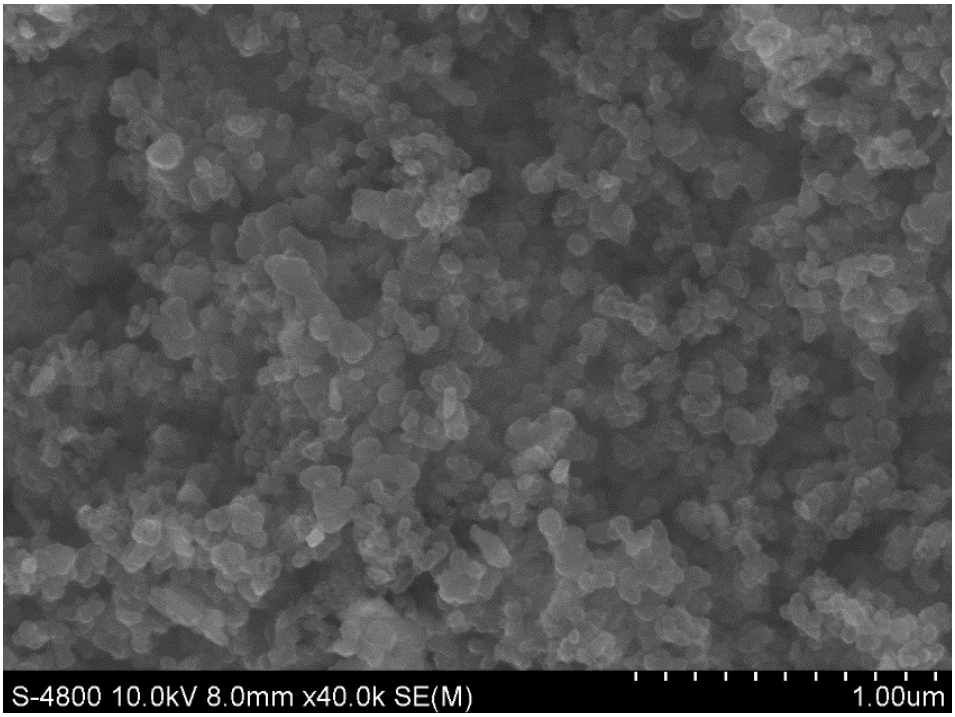

Figure S3. FE-SEM image of the as-obtained $Ti_{0.9}Ir_{0.1}O_2$-C composite.

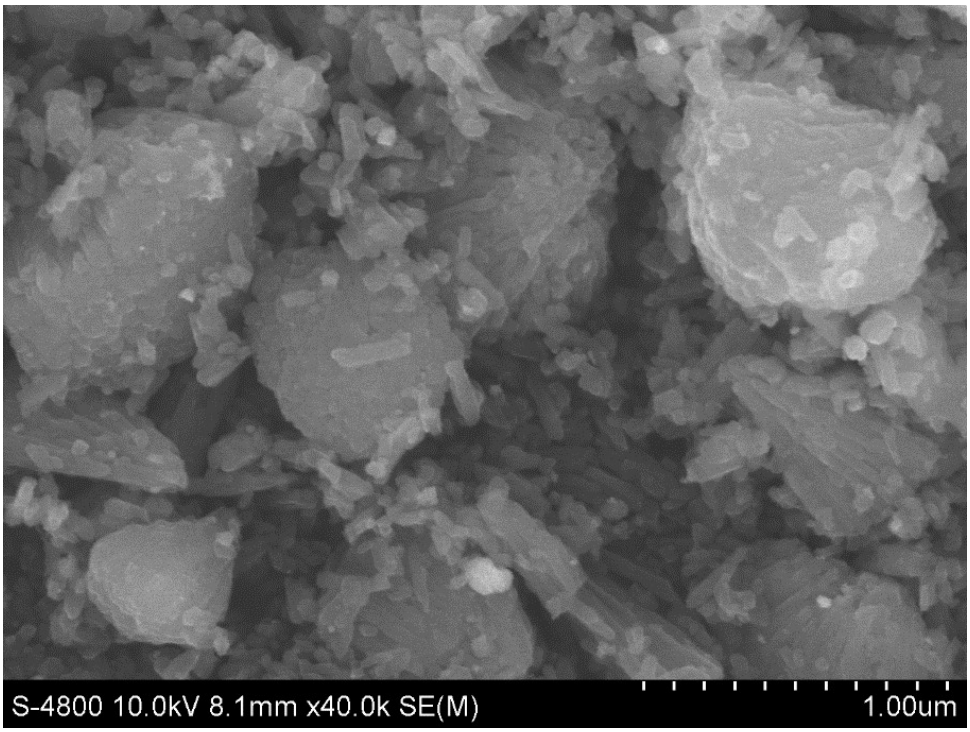

Figure S4. FE-SEM image of the as-obtained $Ti_{0.9}Ir_{0.1}O_2$ support.

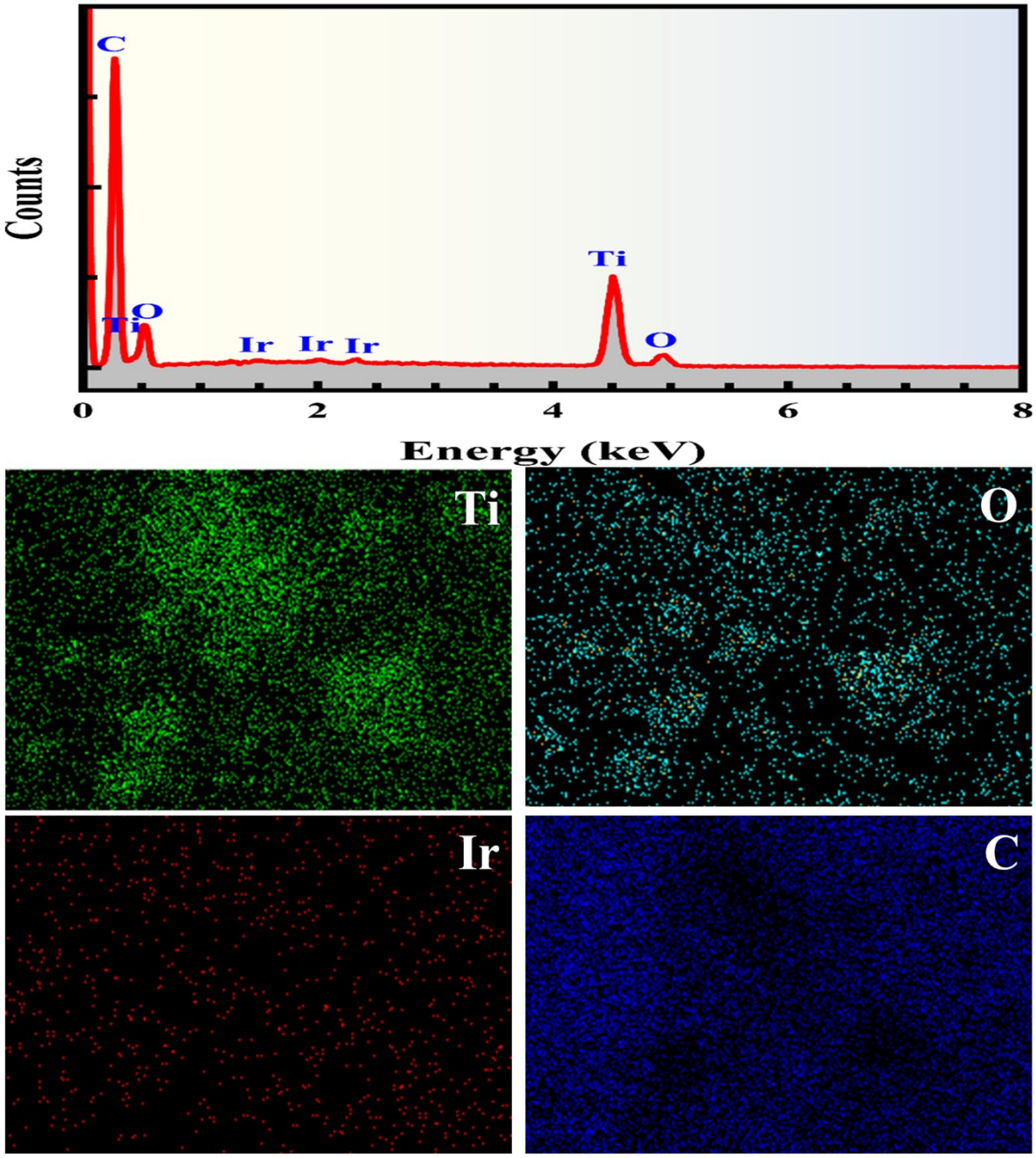

Figure S5. EDX spectroscopy and elemental mapping images of the $Ti_{0.9}Ir_{0.1}O_2$-C composite.

X-ray photoelectron spectroscopy (XPS) was performed to record the chemical state of the elements in the as-made $Ti_{0.9}Ir_{0.1}O_2$-C composite. As illustrated in Figure S6, the Ir 4f XPS spectra were composed of Ir $4f_{5/2}$ (63.32 eV) and Ir $4f_{7/2}$ (60.41 eV), being deconvoluted into two doublet peaks of Ir^{3+} and Ir^{4+} states, which was shifted slightly to energy lower than those of the Ir 4f in IrO_2.[23] The Ti 2p XPS spectra in Figure S7 showed doublet peaks of Ti $2p_{1/2}$ (464.45 eV) and Ti $2p_{3/2}$ (458.75 eV) with a spin-orbital doublet splitting of 5.70 eV, being

assigned to the Ti^{4+} states. By contrast with the energy tendency of Ir 4f, the Ti 2p position was observed at an energy higher than those of the Ti 2p in TiO_2,[24] which strongly affirmed the doping of iridium into rutile TiO_2 structure.[23] Figure S8 depicts that the O 1s XPS spectra were resolved into oxygen atoms in lattices (O-Ti/O-Ir) at 529.91 eV, carboxylic (C=O) at 530.82 eV, surface hydroxyl species (OH^-) at 531.43 eV, and C-O centered at 532.03 eV.[25, 26] Notably, a small peak was observed at 532.74 eV in the O 1s spectra of the $Ti_{0.9}Ir_{0.1}O_2$-C composite, assigning to the formation of Ti-O-C bond, indicating the strong adsorption of activated carbon onto the loaded $Ti_{0.9}Ir_{0.1}O_2$.[26] In addition, the C 1s XPS spectra was deconvoluted to four peaks of C-C bond (284.69 eV), C-O bond (285.76 eV), C=O bond (286.72 eV), and C-O-Ti bond (288.91 eV),[25, 26] as demonstrated in Figure S9. In brevity, these above XPS results strongly confirmed the composite formation between $Ti_{0.9}Ir_{0.1}O_2$ and activated carbon supports, which was consistent with the XRD and FT-IR results. Table S1-S4 summarized the binding energies of all components in the $Ti_{0.9}Ir_{0.1}O_2$-C composite.

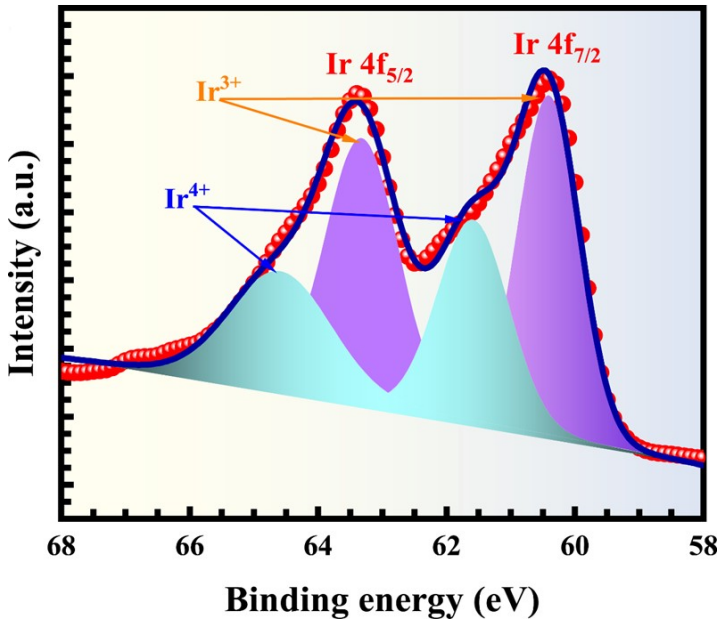

Figure S6. High-resolution XPS spectrums of the Ir 4f in the as-made $Ti_{0.9}Ir_{0.1}O_2$-C composite.

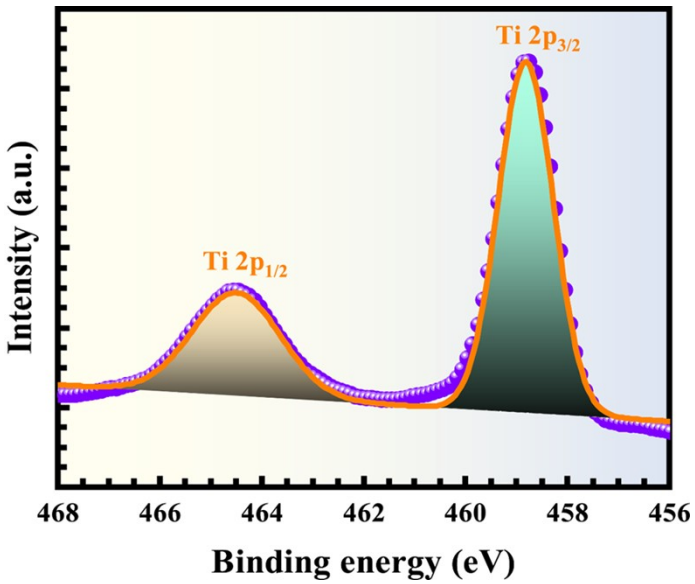

Figure S7. High-resolution XPS spectrums of the Ti 2p in the $Ti_{0.9}Ir_{0.1}O_2$-C composite.

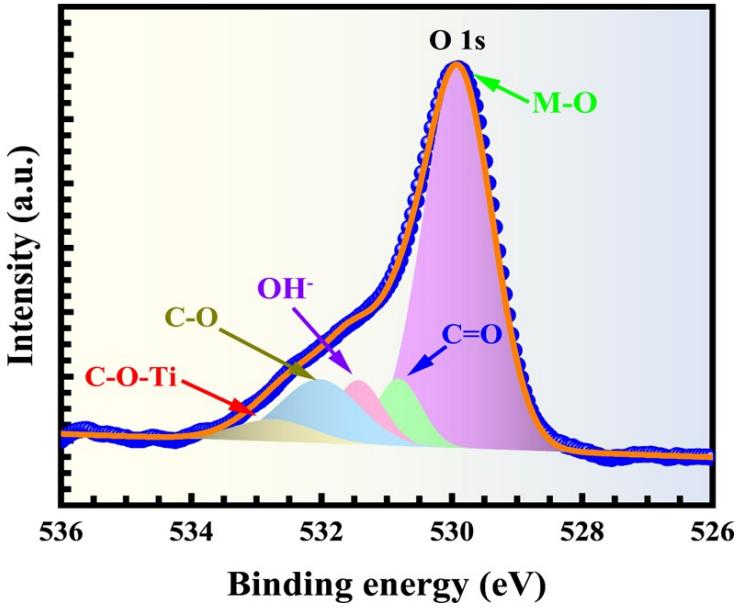

Figure S8. High-resolution XPS spectrums of the O 1s in the $Ti_{0.9}Ir_{0.1}O_2$-C composite.

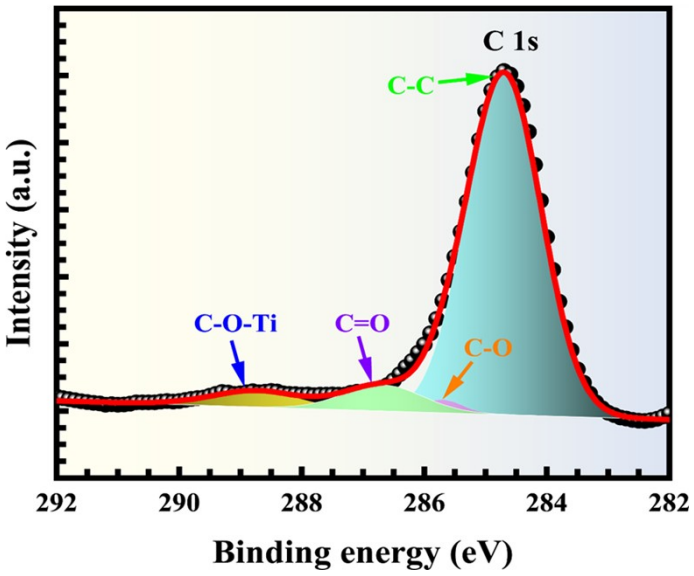

Figure S9. High-resolution XPS spectrums of the C 1s in the $Ti_{0.9}Ir_{0.1}O_2$-C composite.

Furthermore, electrochemical tests (such as CV, EIS, and ADT) were carried out to investigate the efficiency of the as-made $Ti_{0.9}Ir_{0.1}O_2$-C support for the electrochemical process, as shown in Figure S10 – S14. As a result, the $Ti_{0.9}Ir_{0.1}O_2$-C composite was promising catalyst support, for example, the $Ti_{0.9}Ir_{0.1}O_2$-C support exhibited a large double-layer capacitance and high charge transfer efficiency among investigated catalyst supports, suggesting more active sites and efficient electron transfer of the $Ti_{0.9}Ir_{0.1}O_2$-C support during electrochemical reactions. The electrochemical durability of the $Ti_{0.9}Ir_{0.1}O_2$-C support was greater than the Vulcan XC-72 carbon black. The above difference of the $Ti_{0.9}Ir_{0.1}O_2$-C composite support could be interpreted due to the combination of the high conductivity of carbon and the superior electrochemical corrosion resistance of TiO_2-based nanomaterials.[27, 28] What's more, the formation of more interfacial interaction between metal oxides and carbon in the composite supports, which can enhance the electrocatalytic water-splitting reaction.[27, 29, 30]

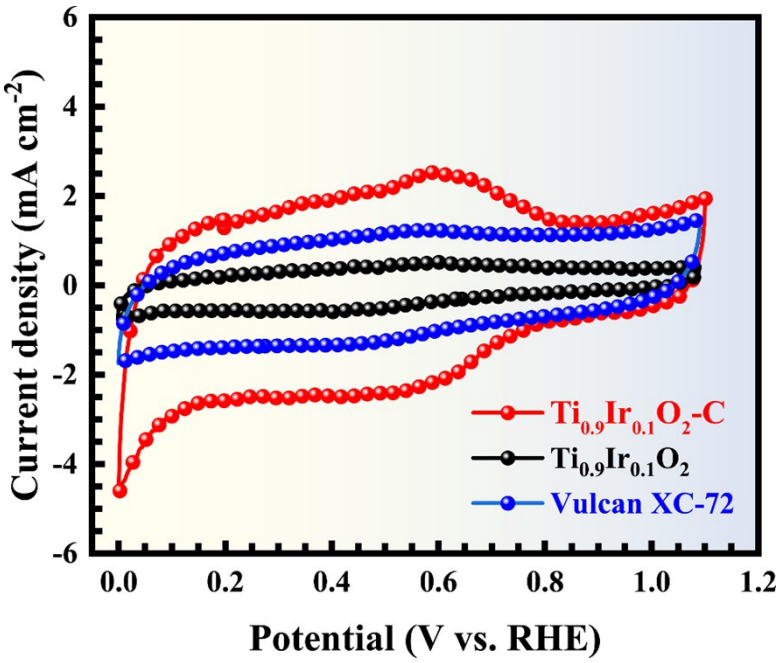

Figure S10. CV curves of all investigated supports in N_2-saturated 0.5 M H_2SO_4 electrolyte at a scan rate of 50 mV s^{-1}.

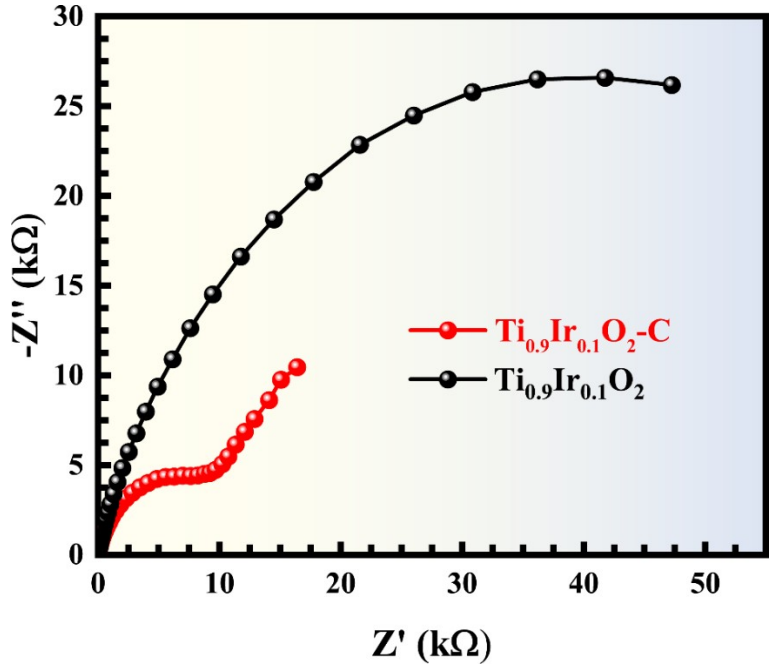

Figure S11. Electrochemical impedance spectroscopy of all studied supports at a potential of 0.0 V_{RHE} in the frequency range from 0.1 to 10^5 Hz in 0.5 M H_2SO_4 electrolyte.

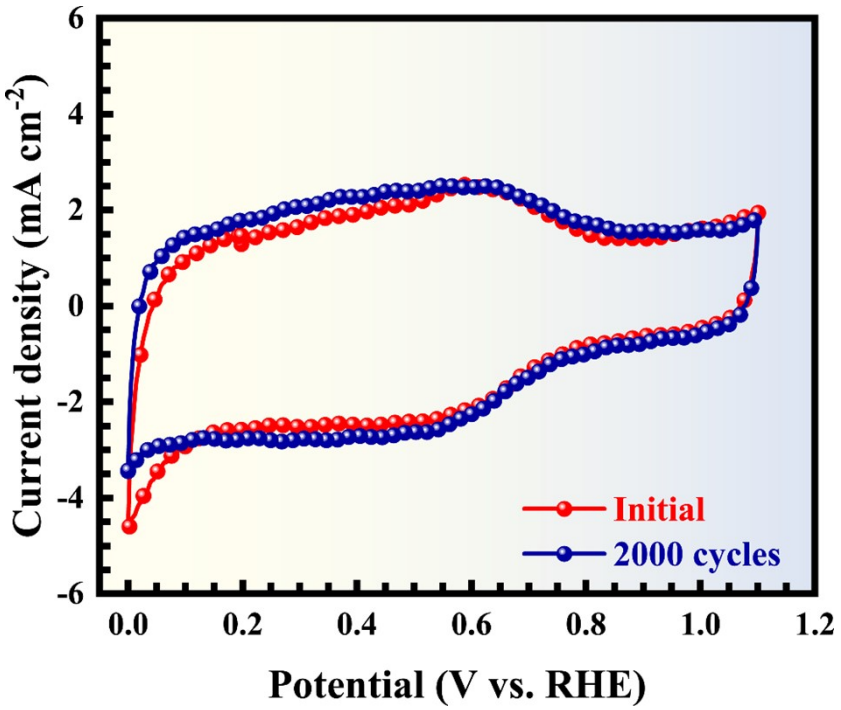

Figure S12. CV curves of the $Ti_{0.9}Ir_{0.1}O_2$-C support before and after the 2000-cycling ADT test at a scan rate of 50 mV s^{-1} in N_2-saturated 0.5 M H_2SO_4 electrolyte.

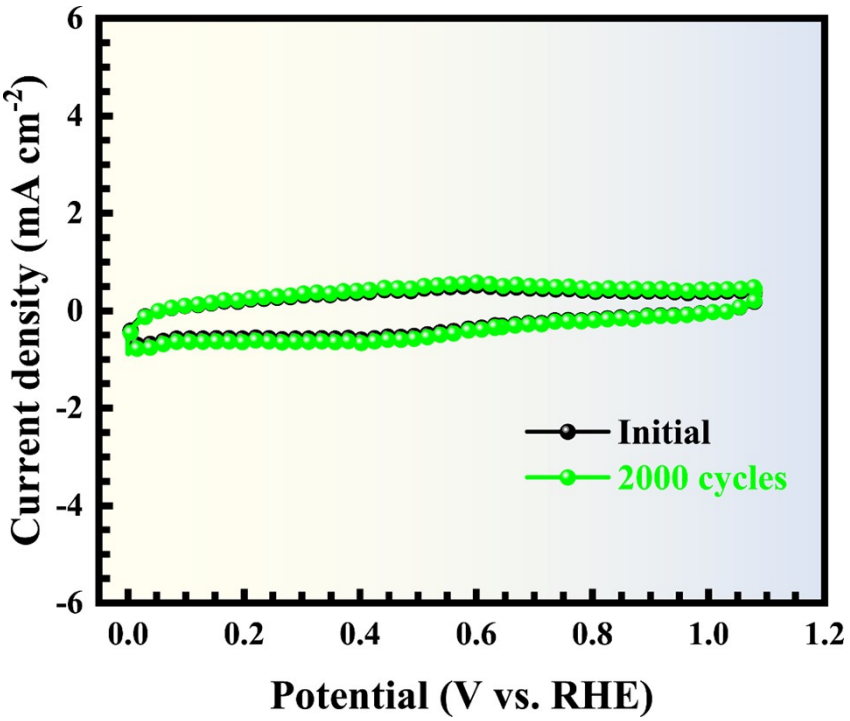

Figure S13. CV curves of the $Ti_{0.9}Ir_{0.1}O_2$ support before and after the 2000-cycling ADT test at a scan rate of 50 mV s^{-1} in N_2-saturated 0.5 M H_2SO_4 electrolyte.

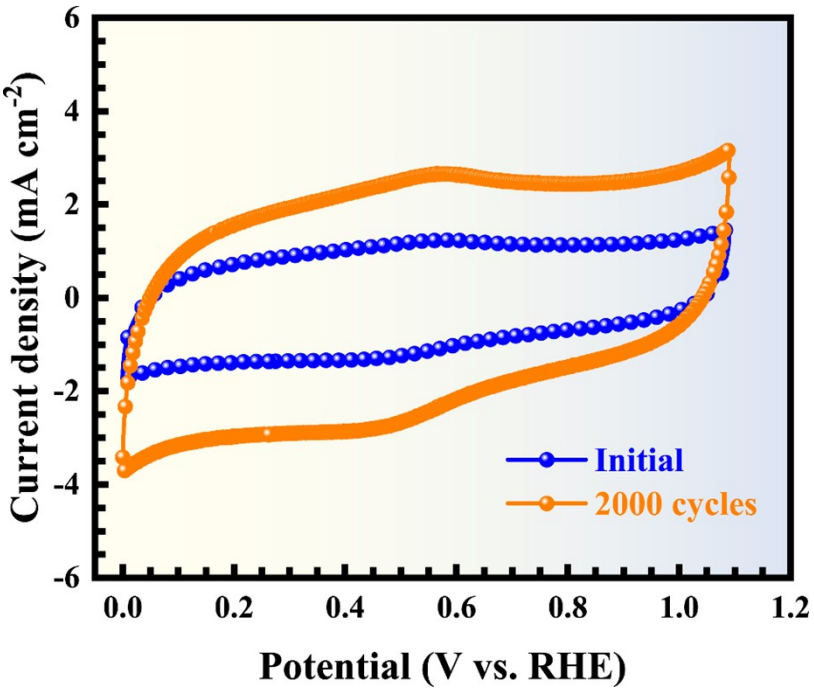

Figure S14. CV curves of the Vulcan XC-72 carbon black support before and after the 2000-cycling ADT test at a scan rate of 50 mV s^{-1} in N_2-saturated 0.5 M H_2SO_4 electrolyte.

Characterization of MoPt/$Ti_{0.9}Ir_{0.1}O_2$-C catalyst

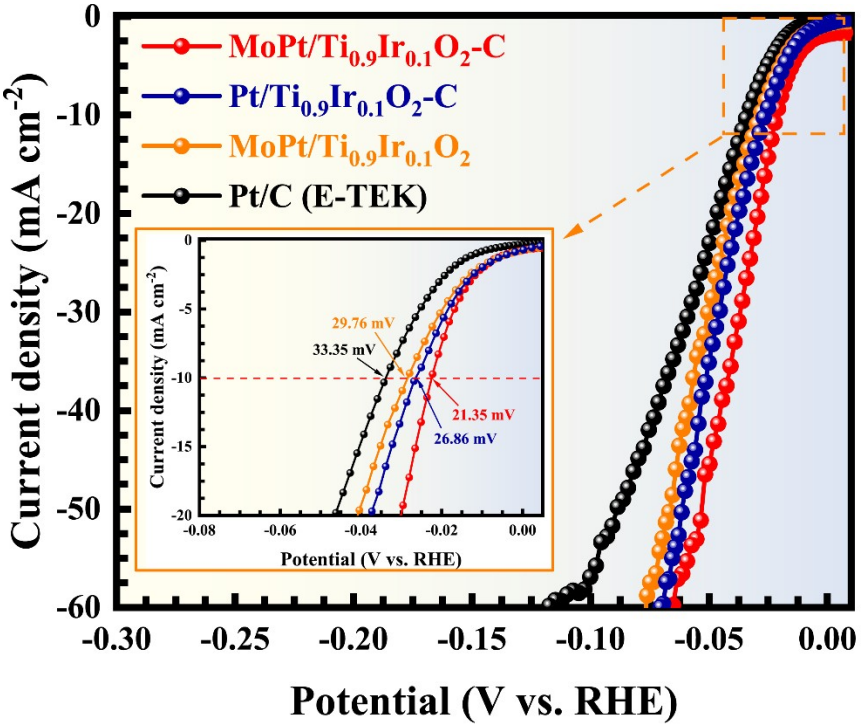

Figure S15. LSV curves of all catalysts in 0.5 M H_2SO_4 electrolyte at a scan rate of 5 mV s^{-1}.

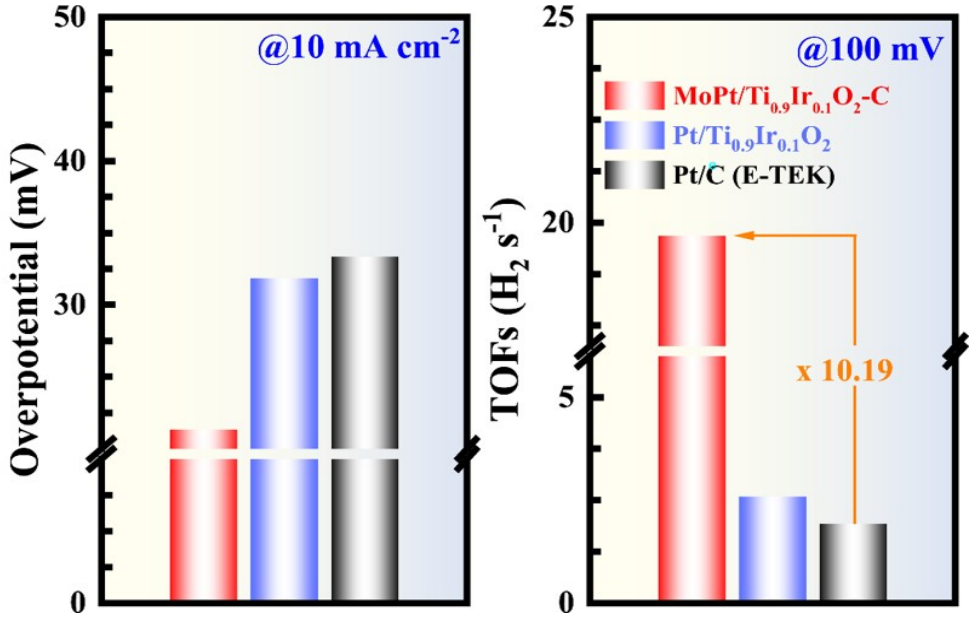

Figure S16. Comparison of overpotential at the current density of 10 mA cm^{-2} and TOFs at a 100 mV potential of different studied HER electrocatalysts in 0.5 M H_2SO_4 electrolyte.

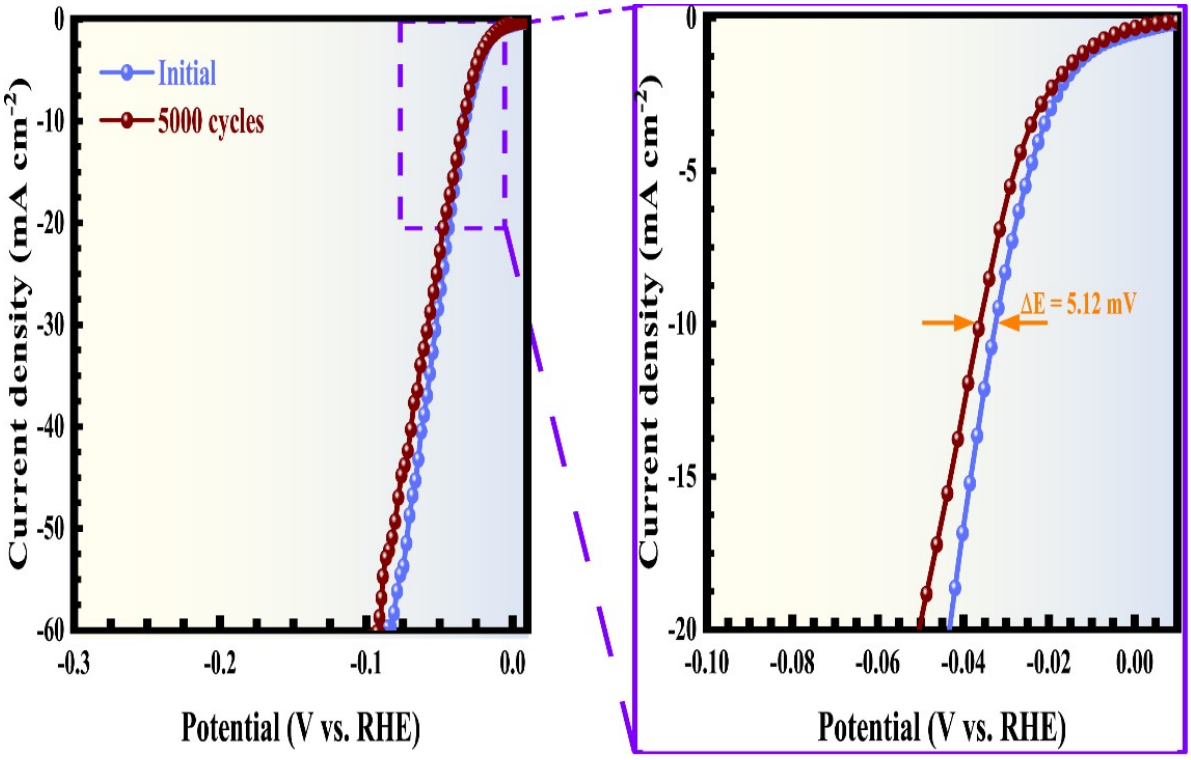

Figure S17. LSV curves of the $Pt/Ti_{0.9}Ir_{0.1}O_2$ catalyst before and after the 5000-cycling ADT test in 0.5 M H_2SO_4 electrolyte solution at a scan rate of 5 mV s^{-1}.

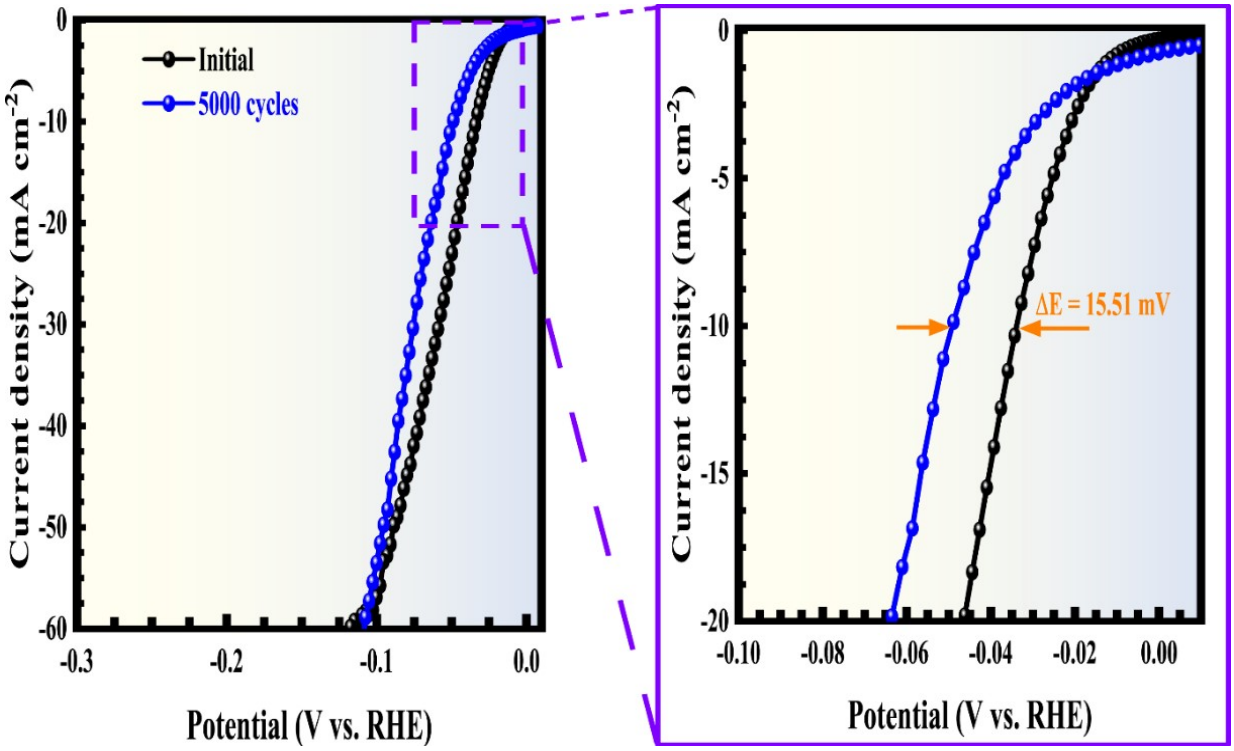

Figure S18. LSV curves of the Pt/C (E-TEK) catalyst before and after the 5000-cycling ADT test in 0.5 M H_2SO_4 electrolyte solution at a scan rate of 5 mV s^{-1}.

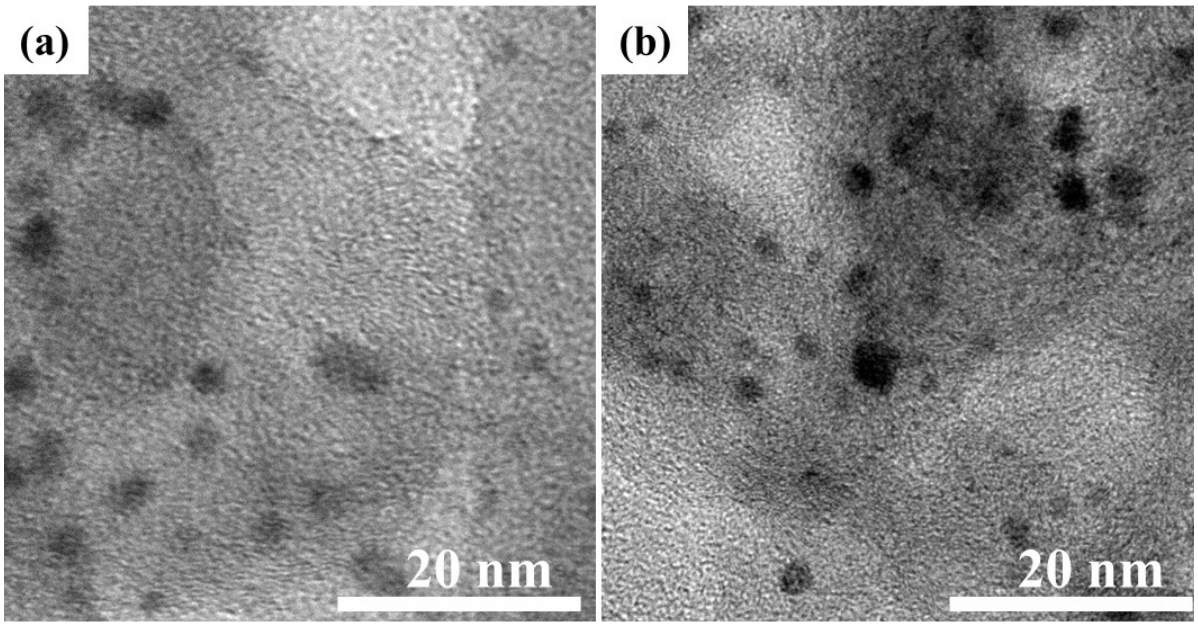

Figure S19. TEM images of the as-made MoPt/$Ti_{0.9}Ir_{0.1}O_2$-C catalyst (a) before and (b) after 5000-cycling ADT in 0.5 M H_2SO_4 electrolyte solution.

Table S1. Comparison of the HER catalytic activity of the as-made MoPt/$Ti_{0.9}Ir_{0.1}O_2$-C catalyst with other reported Pt-based catalysts recently in acidic electrolyte.

Catalysts	Overpotential@ 10 mA cm^{-2} mV	Tafel Slope mV dec^{-1}	Ref.
MoPt/$Ti_{0.9}Ir_{0.1}O_2$-C	21.35	24.01	This work
Pt/$Ti_{0.9}Ir_{0.1}O_2$	31.86	36.72	This work
Pt/C (E-TEK)	33.35	37.31	This work
Pt-Ni_3N/Ni@C	45	47.3	[31]
PtNi/Pt DNPs	21	23	[32]
Pt/$PtTe_2$/$NiCoTe_2$/NPFC HFSs	36	23	[33]
TBA-$Ti_3C_2T_x$-Pt-20	55	70	[34]
Pt-STA-CB	33.8	27.9	[35]
Pt/V_2CT_x	70	20.6	[36]
Pt/Co_3O_4	70	33.5	[37]
Pt/$PtTe_x$ NRs	44	23	[38]
Pt-CNTs	41	49	[39]
Pt_3Fe/BNC	38	31.3	[40]
Pt/NBF-ReS_2/Mo_2CT_x	29	24	[41]
NiO_x@Pt/G	22	20	[42]
PtCo@NC-900	45.5	23	[43]
Pt-PMo/ZIF-67-800	26	30	[44]
Pt_8Co	26.1	34	[45]
Pt@NDPCF	35	36	[46]
Pt/NP-CNT	25	28	[47]
Commercial Pt/C	39	29	[47]
Pt-$Ti_3C_2T_x$ MXene	30	34.8	[48]
PtAg NFs/rGO	55	31	[49]
Pt/$Ti_{0.9}Mo_{0.1}O_2$	26	36	[50]
CuTi@$Pt_{0.24}$ NT	46	33.3	[51]
Pt-MoS_2/MWCNTs	20	15	[52]

References

1. Pham, H. Q.; Huynh, T. T., Rutile $Ti_{0.9}Ir_{0.1}O_2$-Supported Low Pt Loading: An Efficient

Electrocatalyst for Ethanol Electrochemical Oxidation in Acidic Media. *Energy Technology* **2020,** *8* (9), 2000431.

2. Bhuvanendran, N.; Ravichandran, S.; Zhang, W.; Ma, Q.; Xu, Q.; Khotseng, L.; Su, H., Highly efficient methanol oxidation on durable Pt_xIr/MWCNT catalysts for direct methanol fuel cell applications. *International Journal of Hydrogen Energy* **2020,** *45* (11), 6447-6460.

3. Theerthagiri, J.; Cardoso, E. S. F.; Fortunato, G. V.; Casagrande, G. A.; Senthilkumar, B.; Madhavan, J.; Maia, G., Highly Electroactive Ni Pyrophosphate/Pt Catalyst toward Hydrogen Evolution Reaction. *ACS Applied Materials & Interfaces* **2019,** *11* (5), 4969-4982.

4. Wang, N.; Bo, X.; Zhou, M., Single-Step and Room-Temperature Synthesis of Laser-Induced Pt/VC Nanocomposites as Effective Bifunctional Electrocatalysts for Hydrogen Evolution and Oxygen Evolution Reactions. *ACS Applied Materials & Interfaces* **2022,** *14* (20), 23332-23341.

5. Samanta, R.; Panda, P.; Mishra, R.; Barman, S., IrO_2-Modified RuO_2 Nanowires/Nitrogen-Doped Carbon Composite for Effective Overall Water Splitting in All pH. *Energy & Fuels* **2022,** *36* (2), 1015.

6. Wu, J.; Nie, Z.; Xie, R.; Hu, X.; Yu, Y.; Yang, N., Self-assembled Pt–CoFe layered double hydroxides for efficient alkaline water/seawater splitting by spontaneous redox synthesis. *Journal of Power Sources* **2022,** *532*, 231353.

7. McCrory, C. C. L.; Jung, S.; Peters, J. C.; Jaramillo, T. F., Benchmarking Heterogeneous Electrocatalysts for the Oxygen Evolution Reaction. *Journal of the American Chemical Society* **2013,** *135* (45), 16977-16987.

8. Yang, L.; Ren, H.; Liang, Q.; Dinh, K. N.; Dangol, R.; Yan, Q., Ultrathin Amorphous Nickel Doped Cobalt Phosphates with Highly Ordered Mesoporous Structures as Efficient Electrocatalyst for Oxygen Evolution Reaction. *Small* **2020,** *16* (7), 1906766.

9. Wang, B.; Lu, M.; Chen, D.; Zhang, Q.; Wang, W.; Kang, Y.; Fang, Z.; Pang, G.; Feng, S., Ni_xFe_yN@C microsheet arrays on Ni foam as an efficient and durable electrocatalyst for electrolytic splitting of alkaline seawater. *Journal of Materials Chemistry A* **2021,** *9* (23), 13562-13569.

10. Yu, L.; Mishra, I. K.; Xie, Y.; Zhou, H.; Sun, J.; Zhou, J.; Ni, Y.; Luo, D.; Yu, F.; Yu, Y.; Chen, S.; Ren, Z., Ternary $Ni_{2(1-x)}Mo_{2x}P$ nanowire arrays toward efficient and stable hydrogen evolution electrocatalysis under large-current-density. *Nano Energy* **2018,** *53*, 492.

11. Pham, H. Q.; Huynh, T. T., Facile room-temperature fabrication of a silver–platinum nanocoral catalyst towards hydrogen evolution and methanol electro-oxidation. *Materials Advances* **2022,** *3* (3), 1609-1616.

12. Benck, J. D.; Chen, Z.; Kuritzky, L. Y.; Forman, A. J.; Jaramillo, T. F., Amorphous Molybdenum Sulfide Catalysts for Electrochemical Hydrogen Production: Insights into the Origin of their Catalytic Activity. *ACS Catalysis* **2012,** *2* (9), 1916-1923.

13. Kibsgaard, J.; Jaramillo, T. F., Molybdenum Phosphosulfide: An Active, Acid-Stable, Earth-Abundant Catalyst for the Hydrogen Evolution Reaction. *Angewandte Chemie International Edition* **2014,** *53* (52), 14433-14437.

14. Chen, Y.; Ding, R.; Li, J.; Liu, J., Highly active atomically dispersed platinum-based electrocatalyst for hydrogen evolution reaction achieved by defect anchoring strategy. *Applied Catalysis B: Environmental* **2022,** *301*, 120830.

15. Fei, H.; Dong, J.; Arellano-Jiménez, M. J.; Ye, G.; Dong Kim, N.; Samuel, E. L. G.; Peng, Z.; Zhu, Z.; Qin, F.; Bao, J.; Yacaman, M. J.; Ajayan, P. M.; Chen, D.; Tour, J. M., Atomic cobalt on nitrogen-doped graphene for hydrogen generation. *Nature Communications* **2015,** *6* (1), 8668.

16. Huang, T.; Mao, S.; Zhou, G.; Zhang, Z.; Wen, Z.; Huang, X.; Ci, S.; Chen, J., A high-performance catalyst support for methanol oxidation with graphene and vanadium carbonitride. *Nanoscale* **2015,** *7* (4), 1301-1307.

17. Lee, S.; Kim, H. J.; Choi, S. M.; Seo, M. H.; Kim, W. B., The promotional effect of Ni on bimetallic PtNi/C catalysts for glycerol electrooxidation. *Applied Catalysis A: General* **2012,** *429-430*, 39-47.

18. Lee, W.-J.; Bera, S.; Kim, C. M.; Koh, E.-K.; Hong, W.-P.; Oh, S.-J.; Cho, E.; Kwon, S.-H., Synthesis of highly dispersed Pt nanoparticles into carbon supports by fluidized bed reactor atomic layer deposition to boost PEMFC performance. *NPG Asia Materials* **2020,** *12* (1), 40.

19. Zhang, K.; Qiu, J.; Wu, J.; Deng, Y.; Wu, Y.; Yan, L., Morphological tuning engineering of Pt@TiO_2/graphene catalysts with optimal active surfaces of support for boosting catalytic performance for methanol oxidation. *Journal of Materials Chemistry A* **2022,** *10* (8), 4254.

20. Lahkar, S.; Ahmed, S.; Mohan, K.; Saikia, P.; Das, J. P.; Puzari, P.; Dolui, S. K., Iron doped titania/multiwalled carbon nanotube nanocomposite: A robust electrocatalyst for hydrogen evolution reaction in aqueous acidic medium. *Electrochimica Acta* **2022,** *407*, 139921.

21. Hu, J.; Li, H.; Wu, Q.; Zhao, Y.; Jiao, Q., Synthesis of TiO_2 nanowire/reduced graphene oxide nanocomposites and their photocatalytic performances. *Chemical Engineering Journal* **2015,** *263*, 144.

22. Wang, P.; Zhan, S.; Xia, Y.; Ma, S.; Zhou, Q.; Li, Y., The fundamental role and mechanism of reduced graphene oxide in rGO/Pt-TiO_2 nanocomposite for high-performance photocatalytic water splitting. *Applied Catalysis B: Environmental* **2017,** *207*, 335-346.

23. Huynh, T. T.; Tuan Huy, P. C.; Nguyen, H. T. T.; Nguyen, D. T.; Nguyen, S. T.; Pham, H. Q., Tuning crystal structure of iridium-incorporated titanium dioxide nanosupport and its influence on platinum catalytic performance in direct ethanol fuel cells. *Materials Today Chemistry* **2021,** *20*, 100456.

24. Wang, J.; Xu, M.; Zhao, J.; Fang, H.; Huang, Q.; Xiao, W.; Li, T.; Wang, D., Anchoring ultrafine Pt electrocatalysts on TiO_2-C via photochemical strategy to enhance the stability and efficiency for oxygen reduction reaction. *Applied Catalysis B: Environmental* **2018,** *237*, 228.

25. Jiang, Z.-Z.; Wang, Z.-B.; Chu, Y.-Y.; Gu, D.-M.; Yin, G.-P., Ultrahigh stable carbon riveted Pt/TiO_2–C catalyst prepared by in situ carbonized glucose for proton exchange membrane fuel cell. *Energy & Environmental Science* **2011,** *4* (3), 728-735.

26. Fu, X.; Yang, H.; Lu, G.; Tu, Y.; Wu, J., Improved performance of surface functionalized TiO_2/activated carbon for adsorption–photocatalytic reduction of Cr(VI) in aqueous solution. *Materials Science in Semiconductor Processing* **2015,** *39*, 362-370.

27. Ando, F.; Tanabe, T.; Gunji, T.; Tsuda, T.; Kaneko, S.; Takeda, T.; Ohsaka, T.; Matsumoto, F., Improvement of ORR Activity and Durability of Pt Electrocatalyst Nanoparticles Anchored on TiO_2/Cup-Stacked Carbon Nanotube in Acidic Aqueous Media. *Electrochimica Acta* **2017,** *232*, 404.

28. Borbáth, I.; Tálas, E.; Pászti, Z.; Zelenka, K.; Ayyubov, I.; Salmanzade, K.; Sajó, I. E.; Sáfrán, G.; Tompos, A., Investigation of Ti-Mo mixed oxide-carbon composite supported Pt electrocatalysts: Effect of the type of carbonaceous materials. *Applied Catalysis A: General* **2021,** *620*, 118155.

29. Wang, L.; Wu, W.; Lei, Z.; Zeng, T.; Tan, Y.; Cheng, N.; Sun, X., High-performance alcohol electrooxidation on Pt_3Sn–SnO_2 nanocatalysts synthesized through the transformation of Pt–Sn nanoparticles. *Journal of Materials Chemistry A* **2020,** *8* (2), 592-598.

30. Wang, Z.; Wang, L.; Zhu, W.; Zeng, T.; Wu, W.; Lei, Z.; Tan, Y.; Lv, H.; Cheng, N., Pt_3Sn nanoparticles enriched with SnO_2/Pt_3Sn interfaces for highly efficient alcohol electrooxidation. *Nanoscale Advances* **2021,** *3* (17), 5062-5067.

31. Wang, C.; Sun, Y.; Tian, E.; Fu, D.; Zhang, M.; Zhao, X.; Ye, W., Easy access to trace-loading of Pt on inert Ni_3N nanoparticles with significantly improved hydrogen evolution activity at entire pH values. *Electrochimica Acta* **2019,** *320*, 134597.

32. Li, L.; Wang, S.; Xiong, L.; Wang, B.; Yang, G.; Yang, S., Surface-engineered mesoporous Pt nanodendrites with Ni dopant for highly enhanced catalytic performance in hydrogen evolution reaction. *Journal of Materials Chemistry A* **2019,** *7* (20), 12800-12807.

33. Yi, M.; Hu, S.; Lu, B.; Li, N.; Zhu, Z.; Huang, X.; Wang, M.; Zhang, J., Multicomponent

$Pt/PtTe_2/NiCoTe_2$ embedded in ternary heteroatoms-doped carbon for efficient and pH-universal hydrogen evolution reaction. *Journal of Alloys and Compounds* **2021,** *884*, 161042.
34. Yuan, Y.; Li, H.; Wang, L.; Zhang, L.; Shi, D.; Hong, Y.; Sun, J., Achieving Highly Efficient Catalysts for Hydrogen Evolution Reaction by Electronic State Modification of Platinum on Versatile $Ti_3C_2T_x$ (MXene). *ACS Sustainable Chemistry & Engineering* **2019,** *7* (4), 4266-4273.
35. Zhang, T.; Weng, S.; Wang, X.; Zhang, Z.; Gao, Y.; Lin, T.; Zhu, Y.; Zhang, W.; Sun, C., Platinum atomic clusters embedded in polyoxometalates-carbon black as an efficient and durable catalyst for hydrogen evolution reaction. *Journal of Colloid and Interface Science* **2022,** *624*, 704-712.
36. Wang, J.; Guan, Y.; Zhang, Q.; Zhu, H.; Li, X.; Li, Y.; Dong, Z.; Yuan, G.; Cong, Y., Well-dispersed ultrafine Pt nanoparticles anchored on oxygen-rich surface of V_2CT_x (MXene) for boosting hydrogen evolution reaction. *Applied Surface Science* **2022,** *582*, 152481.
37. Jana, R.; Chowdhury, C.; Malik, S.; Datta, A., Pt/Co_3O_4 Surpasses Benchmark Pt/C: An Approach Toward Next Generation Hydrogen Evolution Electrocatalyst. *ACS Applied Energy Materials* **2019,** *2* (8), 5613-5621.
38. Chen, J.; Qin, M.; Ma, S.; Fan, R.; Zheng, X.; Mao, S.; Chen, C.; Wang, Y., Rational construction of $Pt/PtTe_x$ interface with optimal intermediate adsorption energy for efficient hydrogen evolution reaction. *Applied Catalysis B: Environmental* **2021,** *299*, 120640.
39. Zhong, W.; Tu, W.; Wang, Z.; Lin, Z.; Xu, A.; Ye, X.; Chen, D.; Xiao, B., Ultralow-temperature assisted synthesis of single platinum atoms anchored on carbon nanotubes for efficiently electrocatalytic acidic hydrogen evolution. *Journal of Energy Chemistry* **2020,** *51*, 280-284.
40. Qiao, Y.; Cui, J.; Qian, F.; Xue, X.; Zhang, X.; Zhang, H.; Liu, W.; Li, X.; Chen, Q., Pt_3Fe Nanoparticles on B,N-Codoped Carbon as Oxygen Reduction and pH-Universal Hydrogen Evolution Electrocatalysts. *ACS Applied Nano Materials* **2022,** *5* (1), 318-325.
41. Yi, M.; Li, N.; Lu, B.; Li, L.; Zhu, Z.; Zhang, J., Single-atom Pt decorated in heteroatom (N, B, and F)-doped ReS_2 Grown on Mo_2CTx for efficient pH-universal hydrogen evolution reaction and flexible Zn–air batteries. *Energy Storage Materials* **2021,** *42*, 418-429.
42. Shao, F.-Q.; Feng, J.-J.; Yang, Z.-Z.; Chen, S.-S.; Yuan, J.; Wang, A.-J., Cytosine assisted aqueous synthesis of AgPt hollow alloyed nanostructures as highly active electrocatalyst for ethylene glycol oxidation and hydrogen evolution. *International Journal of Hydrogen Energy* **2017,** *42* (39), 24767.
43. Guo, J.; Liu, J.; Mao, X.; Chu, S.; Zhang, X.; Luo, Z.; Li, J.; Wang, B.; Jia, C.; Qian, D.,

Experimental and Theoretical Insights into Enhanced Hydrogen Evolution over PtCo Nanoalloys Anchored on a Nitrogen-Doped Carbon Matrix. *The Journal of Physical Chemistry Letters* **2022,** *13* (23), 5195-5203.

44. Wang, S.; Cao, Y.; Jia, W.; Lu, Z.; Jia, D., A cage-confinement strategy to fabricate Pt-Mo_6Co_6C heterojunction for highly efficient PH-universal hydrogen evolution. *Applied Catalysis B: Environmental* **2021,** *298*, 120579.

45. Hu, J.; Fang, C.; Jiang, X.; Zhang, D.; Cui, Z., PtMn/PtCo alloy nanofascicles: robust electrocatalysts for electrocatalytic hydrogen evolution reaction under both acidic and alkaline conditions. *Inorganic Chemistry Frontiers* **2020,** *7* (22), 4377-4386.

46. Xiao, Y.-X.; Ying, J.; Chen, J.-B.; Dong, Y.; Yang, X.; Tian, G.; Wu, J.; Janiak, C.; Ozoemena, K. I.; Yang, X.-Y., Confined Ultrafine Pt in Porous Carbon Fibers and Their N-Enhanced Heavy d-π Effect. *Chemistry of Materials* **2022,** *34* (8), 3705-3714.

47. Han, J.; Gong, C.; He, C.; He, P.; Zhang, J.; Zhang, Z., Sub-1 nm Pt nanoclusters on N and P co-doped carbon nanotubes for the electrocatalytic hydrogen evolution reaction. *Journal of Materials Chemistry A* **2022,** *10* (31), 16403-16408.

48. Jian, X.; Zhang, M.-m.; Li, R.; Liu, J.-x.; Fu, F.; Liang, Z.-h., Atomically dispersed ultralow-platinum loading on $Ti_3C_2T_x$ MXene as efficient catalyst for hydrogen evolution reaction. *Electrochimica Acta* **2022,** *411*, 140091.

49. Liu, Q.; He, Y.-M.; Weng, X.; Wang, A.-J.; Yuan, P.-X.; Fang, K.-M.; Feng, J.-J., One-pot aqueous fabrication of reduced graphene oxide supported porous PtAg alloy nanoflowers to greatly boost catalytic performances for oxygen reduction and hydrogen evolution. *Journal of Colloid and Interface Science* **2018,** *513*, 455-463.

50. Chen, K.; Deng, S.; Lu, Y.; Gong, M.; Hu, Y.; Zhao, T.; Shen, T.; Wang, D., Molybdenum-doped titanium dioxide supported low-Pt electrocatalyst for highly efficient and stable hydrogen evolution reaction. *Chinese Chemical Letters* **2021,** *32* (2), 765-769.

51. Chuyen Phan, T.; Nguyen, V.-T.; Choi, H.-S.; Kim, H., Highly Efficient and Durable Electrochemical Hydrogen Evolution Reaction based on Composition/Shape Controlled CuTi@Pt Core-Shell Nanotubes in Acidic Media. *Applied Surface Science* **2022**, 154331.

52. Fan, A.; Zheng, P.; Qin, C.; Zhang, X.; Dai, X.; Ren, D.; Fang, X.; Luan, C.; Yang, J., Few-layer MoS_2 and Pt nanoparticles Co-anchored on MWCNTs for efficient hydrogen evolution over a wide pH range. *Electrochimica Acta* **2020,** *358*, 136927.